Surface & Coatings Technology xxx (2015) xxx–xxx

Contents lists available at ScienceDirect

Surface & Coatings Technology

journal homepage: www.elsevier.com/locate/surfcoat

Self-organized TiO_2 nanotube layer on Ti–6Al–7Nb for biomedical application

A.R. Rafieerad [a,b], E. Zalnezhad [a,b,*], A.R. Bushroa [a,b], A.M.S. Hamouda [c], M. Sarraf [a,b], B. Nasiri-Tabrizi [a,d]

[a] Department of Mechanical Engineering, Faculty of Engineering, University of Malaya, 50603 Kuala Lumpur, Malaysia
[b] Center of Advanced Manufacturing and Material Processing, Department of Engineering, University of Malaya, Kuala Lumpur 50603, Malaysia
[c] Mechanical and Industrial Engineering Department, College of Engineering, Qatar University, P.O. Box 2713, Doha, Qatar
[d] Department of Biomedical Engineering, Faculty of Engineering, University of Malaya, 50603 Kuala Lumpur, Malaysia

ARTICLE INFO

Article history:
Received 6 October 2014
Accepted in revised form 28 January 2015
Available online xxxx

Keywords:
Anodization
Ti–6Al–7Nb
TiO_2 nanotube
Surface wettability

ABSTRACT

In the present study, a self-organized nanotube TiO_2 layer on Ti–6Al–7Nb was fabricated. The influence of acidic electrolytes including glycerol (G) and ethylene glycol (EG) on the anodization, microstructural features and surface wettability was explored. The phase compositions and morphological characteristics were characterized by X-ray diffraction (XRD) and field emission scanning electron microscopy (FE-SEM), respectively. According to the results, due to the intrinsic amorphous feature of ceramic oxide, the characteristic TiO_2 peaks were not detected in the XRD profiles. After annealing in normal atmosphere at 600 °C for 2 h, TiO_2 crystallized and consequently, nanotubular TiO_2 arrays containing anatase and rutile phases formed. From a microstructural point of view, the average length and diameter of the nanotube array ranged from 2.23 to 4.22 μm and 160 to 170 nm, respectively. Besides, the type of acidic electrolyte and subsequent annealing noticeably affected the surface wettability of the products.

1. Introduction

Titanium alloys are widely used as implant materials for failed hard tissue owing to their good physiochemical stability, mechanical integrity, good biocompatibility and excellent corrosion resistance [1]. Commercially pure titanium, Ti–6Al–4 V and Ti–6Al–7Nb alloys are the most favored materials for many biomedical applications [2]. Among them, Ti–6Al–7Nb alloy was developed to achieve the following aims [3]: (i) a dense and stable passive surface layer with the presence of all alloying elements, (ii) high resistance to corrosion, (iii) $\alpha + \beta$ grain structure with the possibility of superplastic deformability, (iv) mechanical properties comparable with those of the high-strength, wrought Ti–6Al–4 V alloy, and (v) economical production of semi-finished materials for implant components [4]. Moreover, cell and tissue responses are affected not only by the chemical properties of the implant surface, but also by the implant's surface topography or roughness. Therefore, various surface modifications can be made to enhance the usefulness of implants [5].

It has been found that implant osseointegration occurs through the natural oxide TiO_2 layer, but it is a long process [6]. Accordingly, to enhance implant bioactivity and bone growth, the surface layer can be modified by sand blasting [7], calcium phosphates coating [8] and chemical approaches like acid etching and alkali treatment [9]. According to literature, generating a self-organized TiO_2 nanotube layer is an appropriate surface modification achievable by various techniques, such as sol-gel method [10], electrophoretic deposition [11] and anodization [12]. Among them, anodization is suitable for creating nanotubular oxide layers for biological applications, as it facilitates the highest layer adhesion strength compared to other techniques [13]. In nanotubular TiO_2 arrays, there are some gaps between adjacent nanotubes (~15 nm), which play an important role in minimizing the interfacial stresses between two joined, dissimilar materials. In addition, these gaps create pathways for body fluid supplies of ions, nutrients and proteins [14]. On the other hand, the nanotubular morphology combined with an anatase structure leads to the formation of apatite layers with a thickness of greater than 6 nm in less than 2 days, while no stable apatite layer was observed on amorphous TiO_2 films [15]. In terms of corrosion resistance, TiO_2 nanotube layers on titanium exhibit better corrosion resistance in simulated bio-fluid than smooth Ti [16]. In fact, the functional specifications of nanotubular arrays may be manipulated by varying the process parameters [15]. For instance, a vertically aligned TiO_2 nanotube array can be fabricated on the surface of titanium substrate by anodization in slightly dissolving fluoride-containing

* Corresponding author at: Department of Mechanical Engineering, Faculty of Engineering Building, University of Malaya, 50603 Kuala Lumpur, Malaysia. Tel.: +60 3 79672652; fax: +60 3 79675317.
E-mail address: erfan@um.edu.my (E. Zalnezhad).
URL:E-mail addresses:E-mail address: http://e.zalnezhad@gmail.com (E. Zalnezhad).

http://dx.doi.org/10.1016/j.surfcoat.2015.01.067
0257-8972/

electrolyte [17]. Electrolytes without fluoride, e.g. sulfuric acid [18], are extensively utilized to create a compact non-porous TiO_2 layer at low potential and porous oxides at high potential due to the oxide's electrical breakdown [19,20].

In this study, a self-organized nanotubular TiO_2 layer on Ti–6Al–7Nb was fabricated. In a comparative study, the influence of acidic electrolytes containing glycerol (G) and ethylene glycol (EG) on anodization was investigated. In addition, the microstructural features, surface wettability and reaction mechanism of the formation of vertically aligned TiO_2 nanotube arrays were explored.

2. Materials and methods

2.1. Preparation of the substrate

Ti–6Al–7Nb plates ($20 \times 10 \times 2$ mm^3, Baoji Liu Wei Special Material and Equipment Produce Co. Ltd China) were used as substrate. Prior to anodization, the samples were polished using SiC emery paper (800–2400grit) and then wet-polished in a diamond slurry. Afterwards, the polished samples were sonicated in acetone for 14 min at 40 W power. The sonicated specimens were washed three times with distilled water and dried at 100 °C for 1 h.

2.2. Anodization of Ti–6Al–7Nb (Fabrication of TiO_2 nanotube arrays)

Anodization was performed in a two-electrode electrochemical cell, in which a graphite rod (D = 7 mm) and the specimens were connected to cathode and anode electrodes, respectively. The distance between the electrodes was fixed at approximately 20 mm in all experiments. Here, the anodization process was carried out using a direct current (DC) power source (Model E3641A, Agilent Technologies, Palo Alto, USA) at a constant potential of 60 V for different anodization times (1 to 6 h). To investigate the influence of acidic electrolytes on the anodization process, two electrolytes were used: (i) sodium fluoride (NaF, R&M Chemical, 0.5 wt%) electrolyte dissolved in a 90:10 solvent of EG (purity > 99 %, Merck) and distilled water, and (ii) sodium fluoride (NaF, R&M Chemical, 0.5 wt%) electrolyte dissolved in a 90:10 solvent of G (purity > 99.5 %, Sigma-Aldrich) and distilled water. After anodization, all specimens were washed with deionized water to remove surface residual materials. Finally, thermal annealing (heating and cooling rate of 10 °C/min) was conducted at 450 and 600 °C for 2 h in normal atmosphere to detect the crystalline phases.

2.3. Characterization of TiO_2 nanotube arrays

The morphological features of the nanotubes were characterized by field emission scanning electron microscope (FESEM, FEI Quanta, 2 kV). Phase composition and purity were investigated by grazing incidence X-ray (GIXRD) analysis with a PANalytical Empyrean X-ray diffractometer (*Cu–Kα* radiation) over a 2θ range from 10° to 80°. Surface hydrophobicity was examined by measuring the contact angles with a sessile drop of deionized water deposited on a specimen's surface. Optical wettability was inspected with a video-based optical contact angle measuring system (OCA 15EC). The volume of the liquid was kept constant (10 μl) through all contact angle measurements of the various samples. Moreover, wettability was evaluated with a dropping velocity of 2 μl/sec, accuracy of ± 1°, temperature of 26 ± 1 °C and relative humidity of 45 ± 5 %.

Grazing-incidence diffraction is a scattering geometry combining the Bragg condition with the conditions for x-ray total external reflection from crystal surfaces. This provides superior characteristics of GID as compared to the other diffraction schemes in the studies of thin surface layers, since the penetration depth of x-rays inside the slab is reduced by three orders of magnitude typically from 1-10 μm to 1-10 nm (10-100 Å).

3. Results and discussion

3.1. Microstructural characterization (FESEM analysis)

Fig. 1a-c show FESEM top view images of as-prepared TiO_2 nanotubes in EG (Fig. 1a and b) and G (Fig. 1c and d) electrolytes. It is clear that the surface of the specimens is not smooth and mainly coated by lamellar solid matter. The low-magnified FESEM images (top view) display that the nanotubes are distributed uniformly over the anodized surfaces, indicating an extensive dispersion of nanotubes (Fig. 1a and c). Besides, high magnitude FESEM images of the surfaces show that the as-prepared nanotubes have an average diameter of 40 nm in both electrolytes (Fig. 1b and d). At the beginning of the anodization, the formation of compact oxide layers on the surface of the sample was dominant as a result of the interaction within O^{2-} and OH^{-}. After that, irregular pits were formed due to localized dissolution of oxide layer and followed by the pits conversion to larger pores, while most of the areas covered with oxide layer. With increasing the anodization time, the compact TiO_2 layer collapsed, after which a porous TiO_2 layer gradually grew and the TiO_2 nanotubular arrays were achieved [21].

Fig. 2 and 3 show the microstructural evolutions of the anodized samples after thermal annealing at 450 and 600 °C for 2 h for EG (Fig. a and b) and G (Fig. c and d), respectively. In general, annealing as one of the most widely used post-fabrication processes enhances crystallinity degree of as-prepared amorphous TiO_2 nanotubes and eliminates surface fluorine to improve cell responses [22]. From this figure, it is clear that the crystallization to highly organized structure occurred during annealing in normal atmosphere. This is the same finding as He et al. where they successfully induced crystallization to the anatase structure at temperatures in the range 550–600 °C [23]. In accordance with FESEM images in Fig. 2a and b, the TiO_2 nanotubes obtained in EG showed an average inner diameter of 160 nm and mean tube wall thickness of 15 nm after annealing at 450 °C. Regarding the anodized samples in G (see Fig. 2c and d), the average inner diameter and wall thickness were 167 and 21 nm, respectively. When the annealing temperature rose to 600 °C (Fig. 3a and c), the nanotubular structures remained stable. However, thickening of TiO_2 nanotubes wall took place due to mass transport involving $Ti4+$ diffusion at the bottom and wall of the TiO_2 nanotubes as shown (see Fig. 3b and d). In fact, the change in morphological features with annealing temperature is most probably related to the excessive diffusion of Ti ion along with the nanotube walls, which induced oxidation and thus thickened the oxide walls [21].

FESEM cross-section images of TiO_2 nanotubular arrays in different electrolytes after annealing at 450 and 600 °C are shown in Fig. 4. During annealing at 450 °C, the surface was completely filled with self-organized nanotubes with the length of 3.71 μm in EG and 2.23 μm in G (Fig. 4a and b). With increasing the annealing temperature to 600 °C, the tubular structure remained stable and the nanotube arrays length reached to 4.22 and 2.25 μm in the case of EG and G, respectively (Fig. 4c and d). As shown in this figure, the TiO_2 nanotubes displayed a bamboo-shaped structure with good density (an important factor contributing to good mechanical properties), which could result in enhanced chemical activity and stronger interactions [24]. These findings show that the microstructural features of the self-organized TiO_2 nanotubular arrays were influenced by the type of electrolyte and subsequent annealing.

3.2. Phase evolution and structural features (XRD analysis)

Fig. 5 shows the XRD patterns of the samples anodized for different times using dissimilar electrolytes. From this figure, the XRD profiles of the as-prepared TiO_2 nanotubes for both electrolytes were composed of seven peaks located approximately at 35°, 38°, 40°, 52.8°, 62.8°, 70.5° and 76° which were attributed, respectively, to the (1 0 0), (0 0 2), (1 0 1), (1 0 2), (1 1 0), (1 1 2) and (2 0 1) orientations of the titanium

Please cite this article as: A.R. Rafieerad, et al., Surf. Coat. Technol. (2015), http://dx.doi.org/10.1016/j.surfcoat.2015.01.067

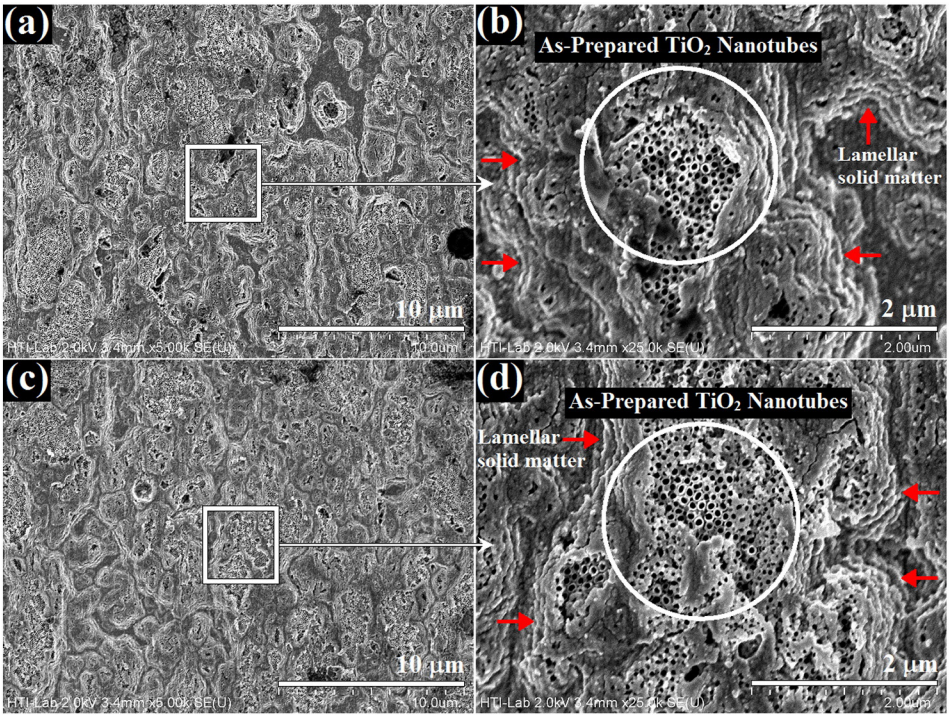

Fig. 1. FESEM top view images of as-prepared TiO_2 nanotubes in different anodization electrolytes, (a,b) EG and (c,d) G.

substrate (JCPDS#005-0682). In fact, no characteristic TiO_2 peaks were observed in the XRD profiles, suggesting that the as-prepared TiO_2 nanotubes were amorphous. Besides, no differences in phase composition were detected between the samples anodized in EG and G.

The XRD patterns of the samples anodized in EG and G after thermal annealing at 600 °C for 2 h are shown in Fig. 6. During annealing at 600 °C (Fig. 6a), the crystallization of TiO_2 layer occurred and consequently the characteristic peaks of TiO_2 with anatase crystalline type (JCPDS#01-071-1166) including (1 0 1) at $2\theta = 25.35°$, (0 0 4) at $2\theta = 37.86°$, (2 0 0) at $2\theta = 48.08°$, (1 0 5) at $2\theta = 53.99°$, and (2 1 1) at $2\theta = 55.06°$ were detected. Besides, some characteristic peaks of titanium were also identified. From the magnified XRD profiles in the ranges of $20° \leq 2\theta \leq 30°$ and $46° \leq 2\theta \leq 50°$ (Fig. 6b and c), it is obvious that the preferential orientation of anatase took place along the (1 0 1) plane for both electrolytes. However, the characteristic TiO_2 peaks has changed

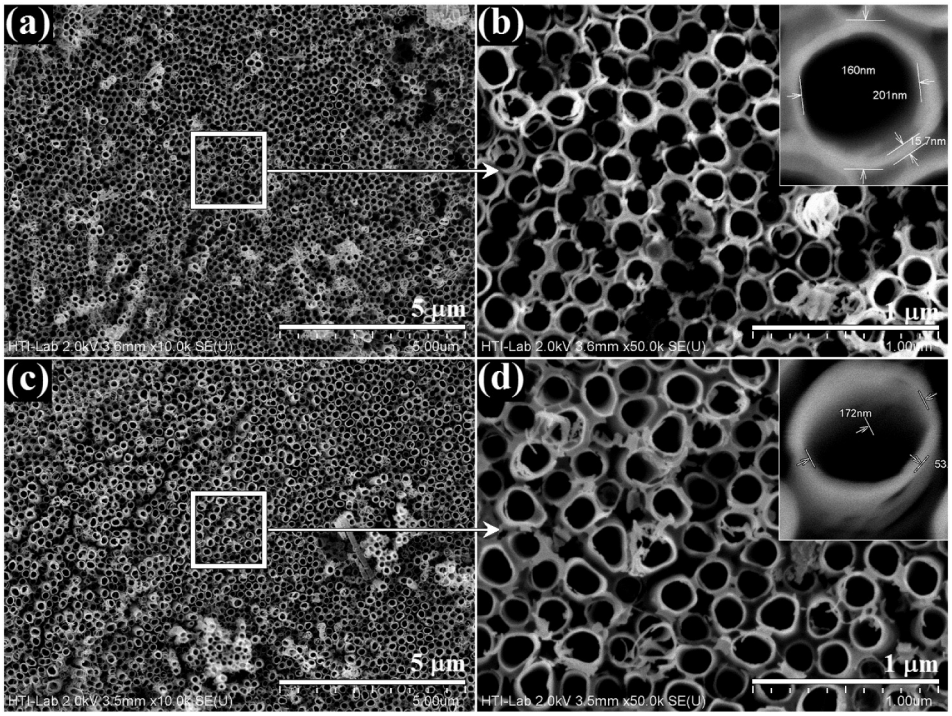

Fig. 2. Microstructural evolutions of the anodized samples after thermal annealing at 450 °C for 2 h, (a,b) EG and (c,d) G.

Please cite this article as: A.R. Rafieerad, et al., Surf. Coat. Technol. (2015), http://dx.doi.org/10.1016/j.surfcoat.2015.01.067

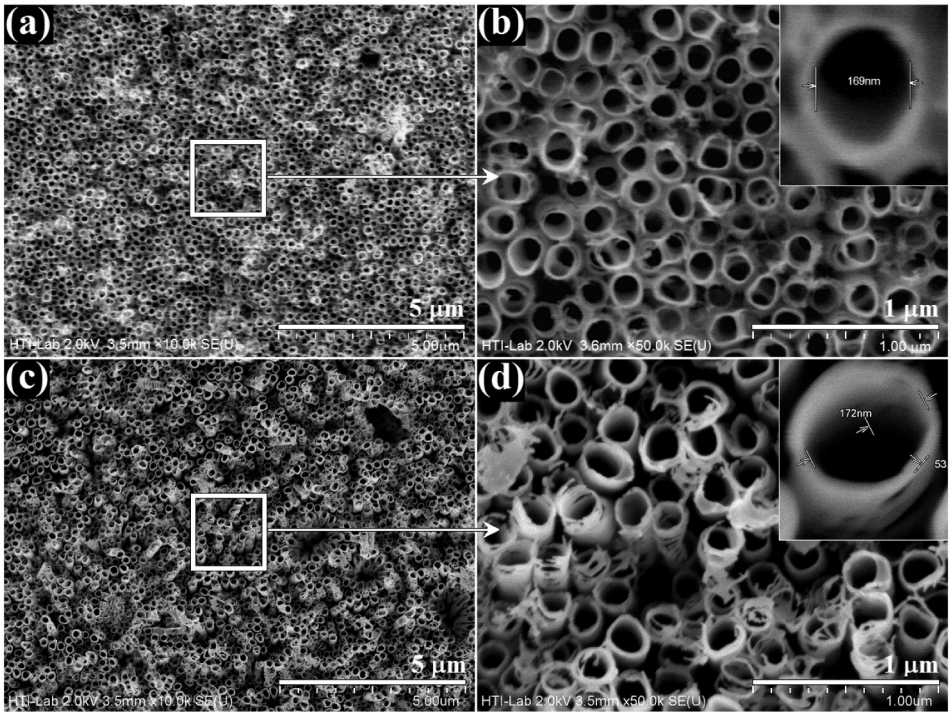

Fig. 3. Microstructural evolutions of the anodized samples after thermal annealing at 600 °C for 2 h, (a,b) EG and (c,d) G.

significantly, indicating that the crystalline phase fraction may be affected by the type of electrolyte. Based on the obtained data, the weight fractions of anatase after annealing at 600 °C were 85 ± 4 and 51 ± 3 % in the case of anodized sample in EG and G, respectively. This result is in good agreement with the previous studies, where the electrolyte composition and subsequent annealing affected on the structural evolutions of TiO_2 nanotubes [25]. For instance, Wang et al. found that in aqueous electrolyte, the anodization potential exerted significant influence on the formation of TiO_2 nanotube arrays, while little effect from the electrolyte temperature was observed. In contrast, in non-aqueous electrolyte, the electrolyte temperature noticeably affected the TiO_2 nanotube dimensions, while the anodization potential showed slight influence in this regard. Moreover, high temperature annealing has been regarded as an effective route to inducing crystalline formation in as prepared TiO_2 nanotube arrays, converting them into the anatase or rutile phase [26].

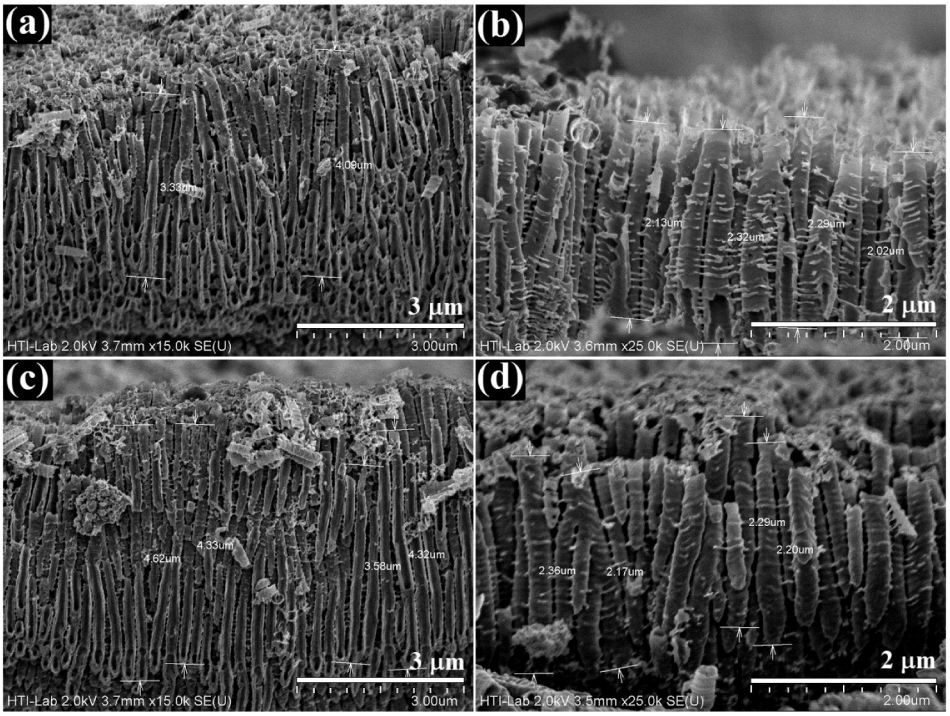

Fig. 4. FESEM cross-section images of TiO_2 nanotubes after 2 h annealing through two electrolytes, (a) EG and (b) G at 450 °C and (c) EG and (d) G at 600 °C.

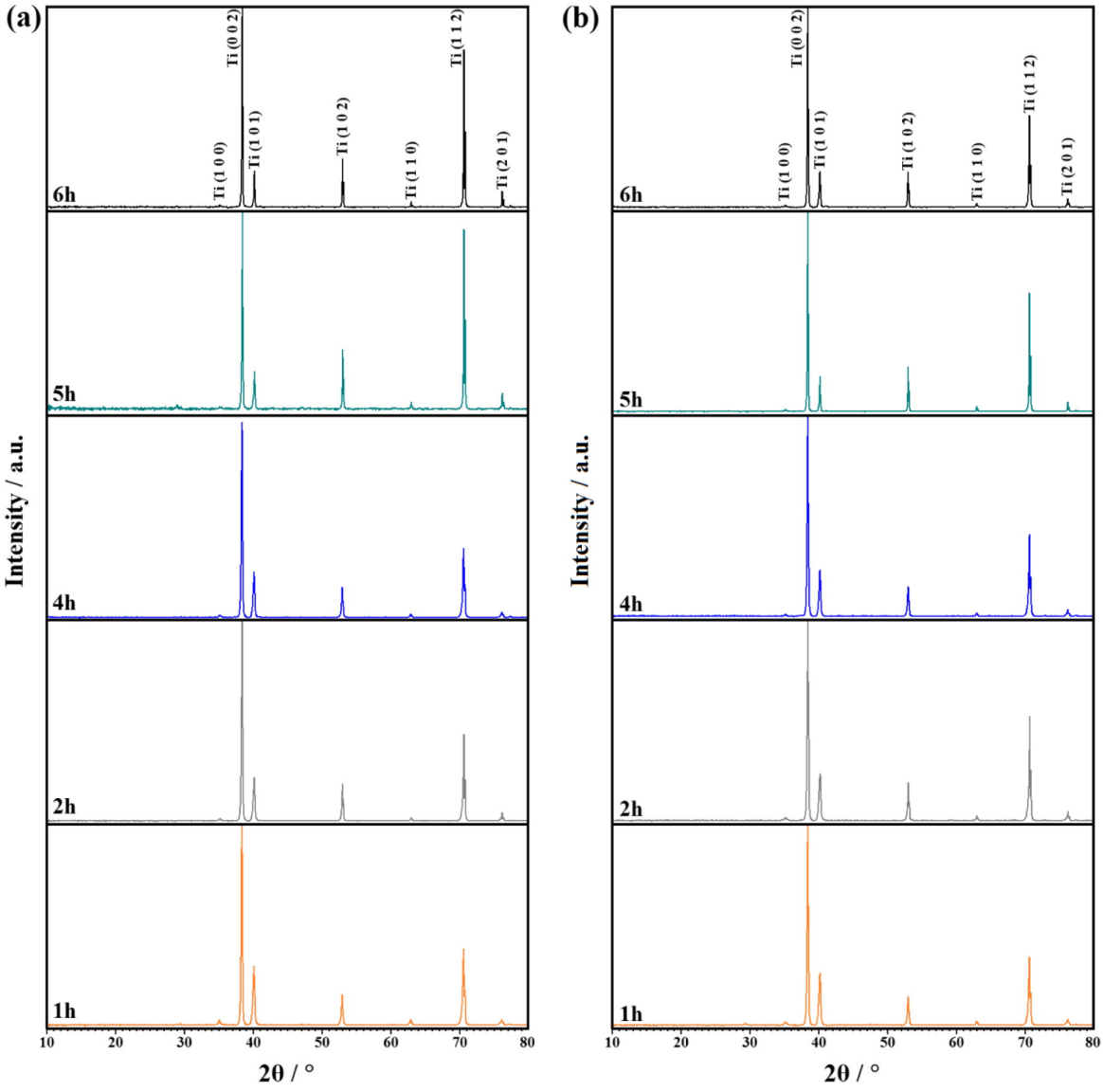

Fig. 5. XRD patterns of the samples anodized for different times using dissimilar electrolytes, (a) EG and (b) G.

3.3. Surface wettability (hydrophilicity)

Anodization on some substrates not only increases the substrate corrosion resistance but also forms nanopores structure films [27,28] that show various surface wettabilities depending on the type of electrolyte. For many approaches, it is desirable to achieve surfaces that can be tuned conveniently between hydrophobicity and hydrophilicity. Thermal annealing as an effectual surface treatment has been effectively utilized to create hydrophilic surfaces owing to high-density oxygen-related defects created by this process [29]. Therefore, in this research work, the surface wettability of anodized samples before and after annealing was examined. Surface wettability is generally a measure of surface energy and is most commonly quantified by a contact angle θ [30]. The drop shape is governed by the action of forces pulling at the drop's contact line on the plane of the solid, where the solid/liquid, liquid/vapor and solid/vapor interfaces meet (Fig. 7a).

Here, the subscripts indicate the three phases: Sis the solid; L is the liquid; and V is the equilibrium vapor. The contact angle is defined by the equilibrium state between the forces acting on the contact line separating wetted and non-wetted portions of a homogenous, smooth, solid surface. Each interface is described by a certain free energy per unit area γ_{SL}, γ_{LV}, and γ_{SV} resulting in Young's equation [31]: $\cos(\theta) = (\gamma_{SV} - \gamma_{SL})/\gamma_{LV}$. It is well-known that electric charge plays a significant role in the wetting phenomenon. The effect, referred to as electrocapillarity—the basis of modern electrowetting and microfluidics, was first described in detail in 1875 by Lippmann [32]. The charges and dipoles redistribute, modifying the surface energy at the liquid drop/substrate interface, when an external electric potential is applied between a liquid drop and solid. As a result, sufficient wetting enhancement was observed. It is described by the modified Young's equation, when the presence of a net electric charge at an interface lowers γ_{SL}. It should be mentioned that the interfacial energies related to γ_{SV} and γ_{LV} remain constant and independent of the applied potential.

In the case of anodized surfaces, the type of electrolyte can also play an important role in the wetting phenomenon. EG has a hydrophilic quality due to the hydrogen bonding. The hydrogen bonding is based on the OH bond in the molecular structure. The dipole-dipole forces among the OH bonds between EG and water bring them together easily [33]. Thus, EG absorbs the water molecule from the air due to the presence of two pairs of OH groups. However, attributable to the high viscosity, G exhibits a hydrophobic surface trait [34]. Based on the

Please cite this article as: A.R. Rafieerad, et al., Surf. Coat. Technol. (2015), http://dx.doi.org/10.1016/j.surfcoat.2015.01.067

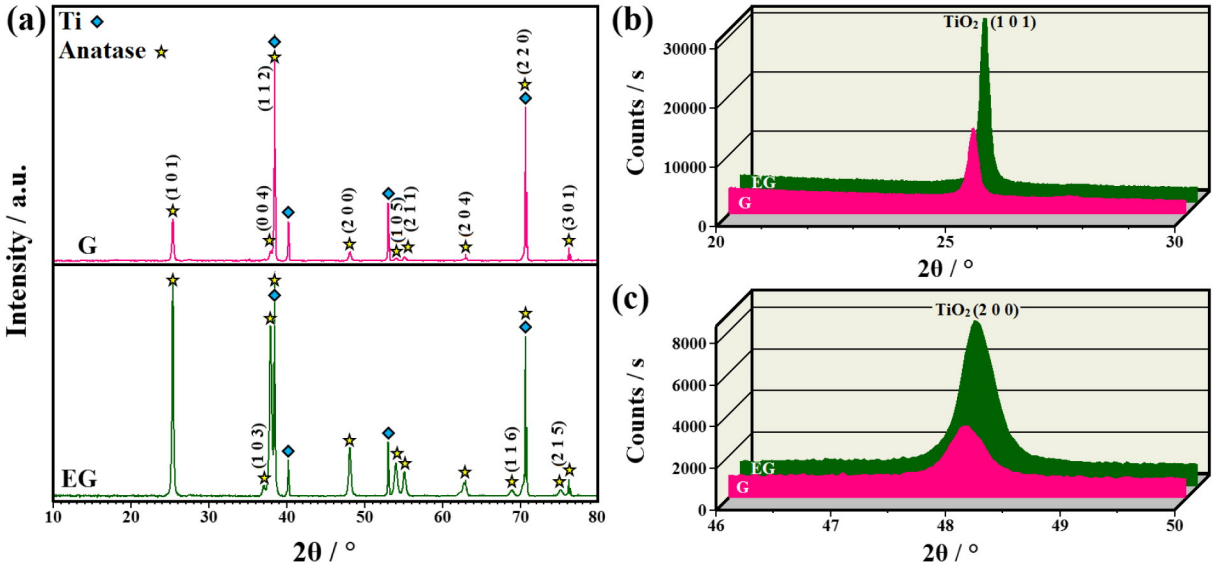

Fig. 6. (a) XRD patterns of the anodized samples in different electrolytes after annealing in normal atmosphere at 600 °C for 2 h and magnified XRD profiles in the ranges of (b) $20° \leq 2\theta \leq 30°$ and (c) $46° \leq 2\theta \leq 50°$.

obtained data, the Ti–6Al–7Nb substrate demonstrated a pronounced hydrophobic state with a contact angle of $\theta = 35.65 \pm 0.002°$ (Fig. 7b). After anodization, the contact angle declined to 14.69 ± 0.002 and $25.93 \pm 0.002°$ in the case of EG and G, respectively. On the other hand, these values changed to $5.61 \pm 0.002°$ and $29.40 \pm 0.002°$ after annealing at 600 °C for 2 h. This signifies that the sort of electrolyte and subsequent thermal treatment considerably influenced the hydrophobic and hydrophilic surface features.

3.4. Formation mechanism of TiO_2 nanotubular array

In general, at the beginning of anodization, field assisted dissolution dominates chemical dissolution since the electric field across the electrode is very high. As the anodization progresses and oxide thickens, the chemical dissolution takes over field assisted dissolution which enhances the size and density of the pores. Then, the growth and propagation of the pores take place by internal motion at the oxide/metal interface which cause the formation of hollow-like cylindrical oxide and finally develop into the nanotubular structure with 80-150 nm diameter and 0.5-25 μm length [35]. However, the physical and chemical properties of nanotube layers can be controlled by changing the fabrication process parameters [15].

It has been found that TiO_2 nanotube array formation in F^--containing electrolyte is a result of the following competing electric field-assisted processes: (1) Ti metal hydrolysis to form TiO_2, (2) dissociation of NaF, and (3) chemical dissolution of TiO_2 at the oxide/electrolyte interface [36]. Fig. 8 shows a schematic of the anodization process and the different stages (1, 2, and 3) of TiO_2 nanotube preparation.

$$Ti^{4+} + 2H_2O \rightarrow TiO_2 + 4H^+ \quad (1)$$

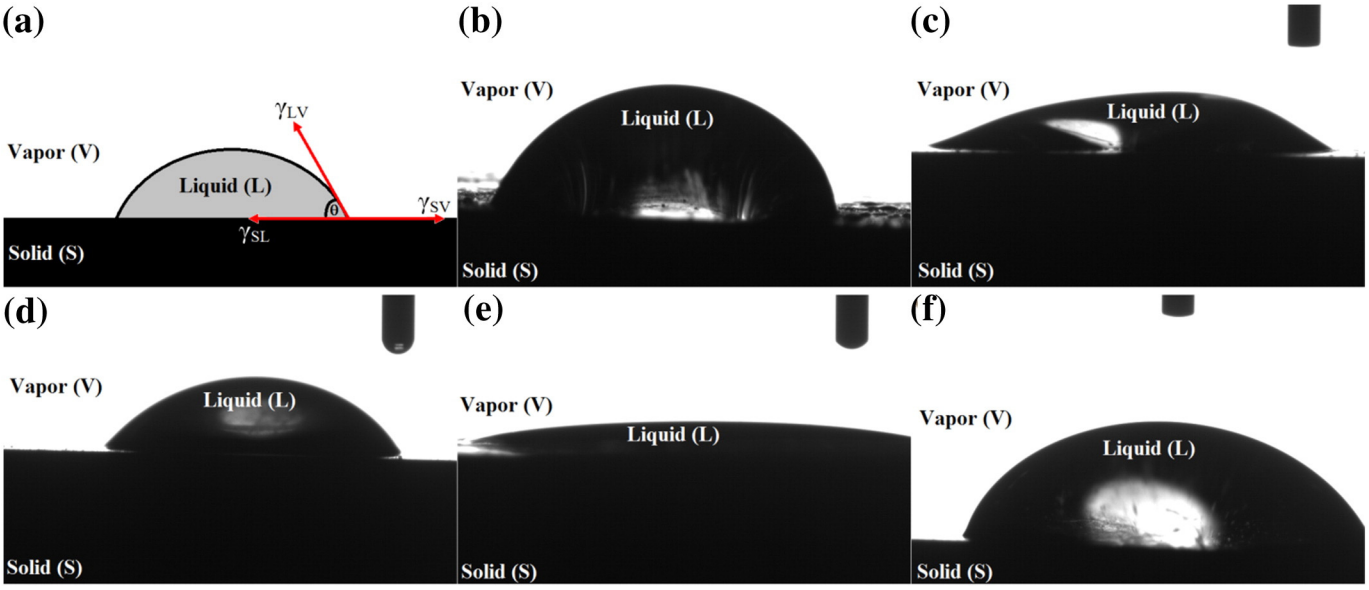

Fig. 7. (a) Schematic view of the wettability effect. The droplet shape is characterized by the contact angle θ, which is defined by three interfacial energies γ_{SV} (surface/vapor), γ_{SL} (surface/liquid), and γ_{LV} (liquid/vapor). Variation of the deionized water contact angle on the (b) substrate, anodized in (c) EG and (d) G as well as anodized samples after annealing at 600 °C for 2 h, (e) EG and (f) G.

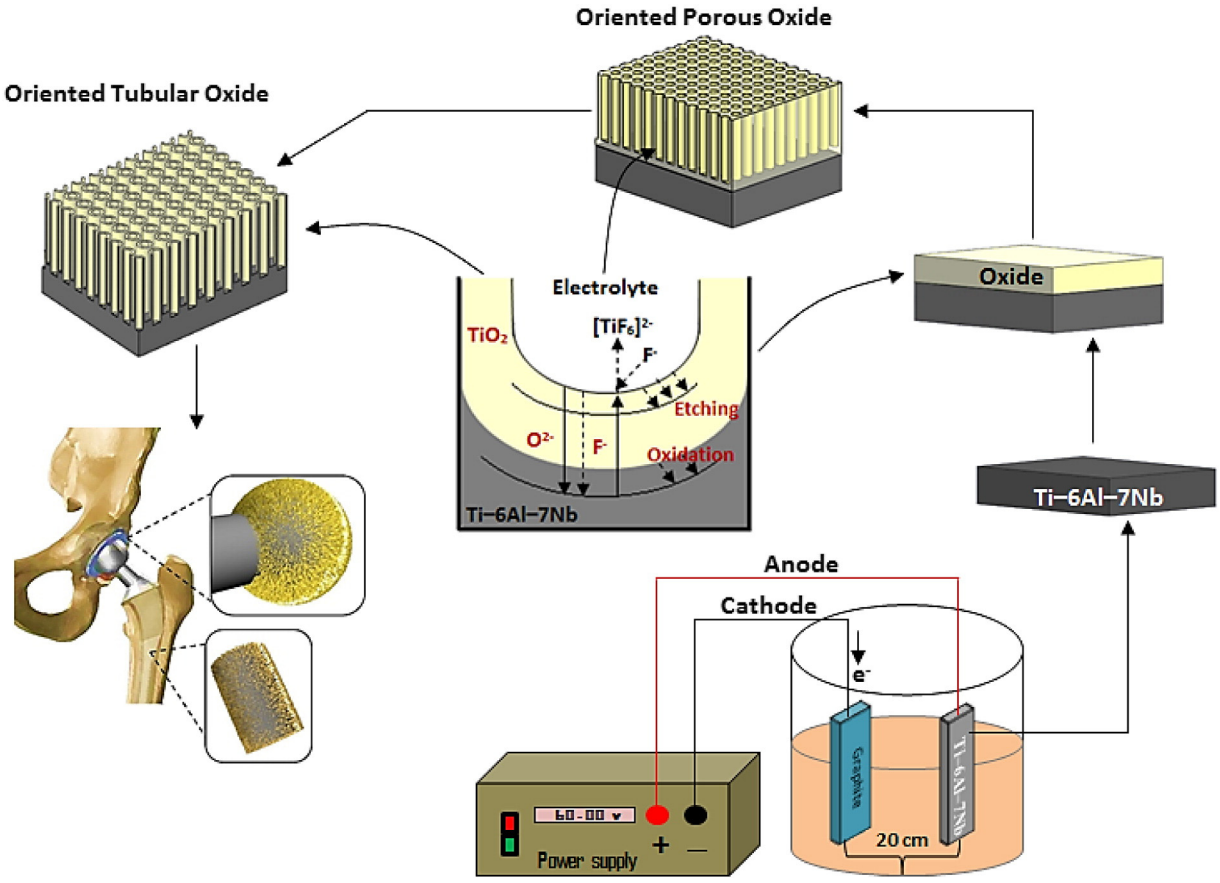

Fig. 8. Schematic view of TiO_2 nanotube formation during anodization in the presence of fluoride [20].

$$NaF \rightarrow Na^+ + F^- \quad (2)$$

$$TiO_2 + 6HF \rightarrow [TiF_6]^2 + 2H_2O + 2H^+ \quad (3)$$

The fabrication process of TiO_2 tube growth involves three stages: 1) An initial barrier layer forms, where there is an exponential decrease in anodic current density until it reaches steady state. The drop in current is caused by the formation of a compact oxide film that enhances resistance and reduces current density. 2) Uniformly distributed pores form, where chemical dissolution of the barrier oxide layer occurs and the current density increases. In this stage, nanopores are generated as a result of random, local dissolution of the TiO_2 surface. 3) Interconnected pores separate into nanotubes and the current density stabilizes again. During this stage, nanotubes form as a result of the simultaneous growth of voids (regions between pores that are susceptible to field-assisted oxidation/dissolution) and pores. In contrast, it has been reported that the separation of pores into individual nanotubes may be a result of the repulsive force between cation vacancies [36–39].

4. Conclusion

In this work, the fabrication of self-organized TiO_2 nanotubular arrays on Ti–6Al–7Nb was studied. The effects of electrolyte type and subsequent annealing on morphological characteristics and surface wettability were investigated. Besides, the reaction mechanism of TiO_2 nanotube formation was evaluated. According to the results, TiO_2 nanotube array formation was a result of competing electric field-assisted processes, including (i) hydrolysis of Ti metal to form TiO_2, (ii) dissociation of NaF, and (iii) chemical dissolution of TiO_2 at the oxide/electrolyte interface. The XRD patterns indicated that TiO_2 with anatase crystalline type was formed after thermal annealing at 600 °C for 2 h, signifying that ceramic oxide layer crystallization occurred during annealing. After annealing at 450 and 600 °C, TiO_2 nanotubular arrays formed. The average inner diameter and mean tube wall thickness ranged from 160 to 170 nm and 15 to 21 nm, respectively. The surface wettability evaluation showed that the hydrophobic and hydrophilic surface features were significantly influenced by the type of electrolyte used and subsequent thermal treatment. To sum up, these study results may contribute to the development of ceramic nanotube arrays on Ti–6Al–7Nb alloy, to be considered in various biomedical applications.

Acknowledgement

The authors would like to acknowledge the University of Malaya for providing the necessary facilities and resources for this research. This work has been supported by the University of Malaya, grant Nos.: UM TNC2/RC/261/1/1/RP021C-13AET and HIR UM.C/HIR/MOHE/ENG/27.

References

[1] M. Geetha, A. Singh, R. Asokamani, A. Gogia, Prog. Mater. Sci. 54 (2009) 397–425.
[2] D. Dunn, S. Raghavan, Surf. Coat. Technol. 50 (1992) 223–232.
[3] M. Semlitsch, Clin. Mater. 2 (1987) 1–13.
[4] M. Shirkhanzadeh, J. Mater. Sci. Mater. Med. 3 (1992) 322–325.
[5] R. Narayanan, S. Seshadri, Corros. Sci. 49 (2007) 542–558.
[6] P. Ducheyne, Q. Qiu, Biomaterials 20 (1999) 2287–2303.
[7] W. Hedzelek, B. Sikorska, L. Domka, Physicochem. Probl. Miner. Process. 39 (2005) 149–154.
[8] F. Variola, J.-H. Yi, L. Richert, J.D. Wuest, F. Rosei, A. Nanci, Biomaterials 29 (2008) 1285–1298.
[9] L. Jonášová, F.A. Müller, A. Helebrant, J. Strnad, P. Greil, Biomaterials 25 (2004) 1187–1194.
[10] T. Maiyalagan, B. Viswanathan, U. Varadaraju, Bull. Mater. Sci. 29 (2006) 705.
[11] K. Raja, M. Misra, K. Paramguru, Mater. Lett. 59 (2005) 2137–2141.
[12] X. Yu, Y. Li, W. Wlodarski, S. Kandasamy, K. Kalantar-Zadeh, Sensors Actuators B Chem. 130 (2008) 25–31.

[13] J.M. Macak, H. Tsuchiya, L. Taveira, A. Ghicov, P. Schmuki, J. Biomed. Mater. Res. Part A 75 (2005) 928–933.
[14] S. Oh, S. Jin, Mater. Sci. Eng. C 26 (2006) 1301–1306.
[15] J. Kunze, L. Muller, J.M. Macak, P. Greil, P. Schmuki, F.A. Muller, Electrochim. Acta 53 (2008) 6995–7003.
[16] W.-q. Yu, J. Qiu, L. Xu, F.-q. Zhang, Biomed. Mater. 4 (2009) 065012.
[17] W.-Y. Zhang, G.-Z. Li, Y.-N. Li, Z.-T. Yu, Z.-P. Xi, Trans. Nonferrous Metals Soc. China 17 (2007) s692–s695.
[18] D.I. Petukhov, A.A. Eliseev, I.V. Kolesnik, K.S. Napolskii, A.V. Lukashin, Y.D. Tretyakov, S.V. Grigoriev, N.A. Grigorieva, H. Eckerlebe, Microporous Mesoporous Mater. 114 (2008) 440–447.
[19] B. Yang, M. Uchida, H.-M. Kim, X. Zhang, T. Kokubo, Biomaterials 25 (2004) 1003–1010.
[20] S. Sobieszczyk, Adv. Mater. Sci. 9 (2009) 25–41.
[21] K.A. Saharudin, S. Sreekantan, S.N.Q.A.A. Aziz, R. Hazan, C.W. Lai, R.B.S.M.N. Mydin, I. Mat, J. Nanosci. Nanotechnol. 12 (2012) 1–10.
[22] K.M. Kummer, E. Taylor, T.J. Webster, Nanosci. Nanotechnol. Lett. 4 (2012) 483–493.
[23] Z. He, J. Xiaoa, F. Xia, Ko. Kajiyoshi, C. Samart, H. Zhang, Appl. Surf. Sci. 313 (2014) 633–639.
[24] S. Baradaran, W. Basirun, E. Zalnezhad, M. Hamdi, A.A. Sarhan, Y. Alias, J. Mech. Behav. Biomed. Mater. 20 (2013) 272–282.
[25] J. Wang, Z. Lin, J. Phys. Chem. C 113 (2009) 4026–4030.
[26] O.K. Varghese, D. Gong, M. Paulose, C.A. Grimes, E.C.J. Dickey, J. Mater. Res. 18 (2003) 156–165.
[27] K. Kobayashi, K. Shimizu, J. Electrochem. Soc. 135 (1988) 908–910.
[28] H. Wang, D. Dai, X. Wu, Appl. Surf. Sci. 254 (2008) 5599–5601.
[29] X.Q. Meng, D.X. Zhao, J.Y. Zhang, D.Z. Shen, Y.M. Lu, L. Dong, Z.Y. Xiao, Y.C. Liu, X.W. Fan, Chem. Phys. Lett. 413 (2005) 450–453.
[30] D. Aronov, A. Karlov, G. Rosenman, J. Eur. Ceram. Soc. 27 (2007) 4181–4186.
[31] T. Young, Philos. Trans. R. Soc. Lond. (1805) 65–87.
[32] G. Lippmann, Gauthier-Villars, 1875.
[33] M. Kao, D. Tien, C. Jwo, T. Tsung, Journal of Physics: Conference Series, IOP Publishing, 2005, p. 442.
[34] O. Rahmanian, C.-F. Chen, D.L. DeVoe, Langmuir 28 (2012) 12923–12929.
[35] Z. Lockmana, S. Sreekantana, S. Ismaila, L. Schmidt-Mendeb, J.L. MacManus-Driscollc, J. Alloys Compd. 503 (2010) 359–364.
[36] G. Crawford, N. Chawla, K. Das, S. Bose, A. Bandyopadhyay, Acta Biomater. 3 (2007) 359–367.
[37] G. Mor, O.K. Varghese, M. Paulose, N. Mukherjee, C.A. Grimes, J. Mater. Res. 18 (2003) 2588–2593.
[38] V. Prida, E. Manova, V. Vega, M. Hernandez-Velez, P. Aranda, K. Pirota, M. Vázquez, E. Ruiz-Hitzky, J. Magn. Magn. Mater. 316 (2007) 110–113.
[39] K. Raja, M. Misra, K. Paramguru, Electrochim. Acta 51 (2005) 154–165.

Please cite this article as: A.R. Rafieerad, et al., Surf. Coat. Technol. (2015), http://dx.doi.org/10.1016/j.surfcoat.2015.01.067